A MXene-Based Hierarchical Design Enabling Highly Efficient and Stable Solar-Water Desalination with Good Salt Resistance

Xiangqian Fan, Yang Yang, Xinlei Shi, Yang Liu, Hongpeng Li, Jiajie Liang,* and Yongsheng Chen

A solar-thermal water evaporation structure that can continuously generate clean water with high efficiency and good salt rejection ability under sunlight is highly desirable for water desalination, but its realization remains challenging. Here, a hierarchical solar-absorbing architecture is designed and fabricated, which comprises a 3D MXene microporous skeleton with vertically aligned MXene nanosheets, decorated with vertical arrays of metal–organic framework-derived 2D carbon nanoplates embedded with cobalt nanoparticles. The rational integration of three categories of photothermal materials enables broadband light absorption, efficient light to heat conversion, low heat loss, rapid water transportation behavior, and much-improved corrosion and oxidation resistance. Moreover, when assembling with a hydrophobic insulating layer with hydrophilic channel, the MXene-based solar absorber can exhibit effective inhibition of salt crystallization due to the ability to advect and diffuse concentrated salt back into the water. As a result, when irradiating under one sun, the solar-vapor conversion efficiency of the MXene-based hierarchical design can achieve up to ≈93.4%, and can remain over 91% over 100 h to generate clean vapor for stable and continuous water desalination. This strategy opens an avenue for the development of MXene-based solar absorbers for sustainable solar-driven desalination.

X. Fan, X. Shi, Dr. Y. Liu, Dr. H. Li, Prof. J. Liang
School of Materials Science and Engineering
National Institute for Advanced Materials
Nankai University
Tianjin 300350, P. R. China
E-mail: liang0909@nankai.edu.cn
Dr. Y. Yang, Prof. J. Liang, Prof. Y. Chen
Key Laboratory of Functional Polymer Materials of Ministry of Education
College of Chemistry
Nankai University
Tianjin 300350, P. R. China
Dr. Y. Yang
The Institute of Seawater Desalination and Multipurpose Utilization
Ministry of Natural Resources (Tianjin)
Tianjin 300192, P. R. China
Prof. J. Liang
Tianjin Key Laboratory of Metal and Molecule-Based Material Chemistry
and Collaborative Innovation Center of Chemical Science and
Engineering (Tianjin)
Nankai University
Tianjin 300350, P. R. China

The ORCID identification number(s) for the author(s) of this article can be found under https://doi.org/10.1002/adfm.202007110.

DOI: 10.1002/adfm.202007110

1. Introduction

Although water is the most abundant resource on Earth, the shortage of readily available freshwater has always been a critical bottleneck for the development and maintenance of functioning societies.[1–5] To combat this issue, desalination and sewage treatment processes have been developed to remove salt and waste from seawater and wastewater to create freshwater.[6,7] However, to enable these processes, an energy source is required. Solar energy is the theoretical energy source that is the most abundant, renewable and inexhaustible, and can be employed for various applications spanning photovoltaics,[8] photocatalysis,[9] solar to heat conversion[10] etc. In particular, solar to heat conversion has been demonstrated to have the highest energy convergence efficiency amongst all solar energy harvesting technologies.[11–13] Due in part to this high solar to heat conversion efficiency, solar-thermal water evaporation, which absorbs and converts solar energy into heat through a solar absorber for vapor generation, is considered to be one of the most effective and simple technique for water desalination and wastewater purification.[14–18]

Though vapor generation is known to result in relatively high conversion efficiency, there is still much focus on developing techniques to further improve efficiency metrics. To enable efficient solar-vapor generation, the solar absorber should have a high solar to thermal conversion efficiency, defined as $\eta = mh_{fg}/q_{solar}A$, wherein m represents the mass flux of vapor, h_{fg} is the enthalpy of the liquid to vapor phase change, q_{solar} is the solar flux per area, and A denotes the surface area of the absorber exposed to the sun.[19] This equation can be additionally expressed and broken down as $mh_{fg} = A\alpha q_{solar} - Aq_{water} - Ah(T - T_\infty) - A\varepsilon\sigma(T^4 - T_\infty^4)$, wherein α is the solar absorbance of the solar absorber (a photothermal material), q_{water} is the heat flux (including conduction and radiation) to the underlying water, h is the convection heat transfer coefficient, ε is the emittance of the absorbing surface, σ is the Stefan–Boltzmann constant, T is the temperature of solar absorber, and T_∞ is the environmental temperature.[20] Based on this equation, it can be deduced that the pathway to achieve

**ADVANCED
SCIENCE NEWS**
www.advancedsciencenews.com
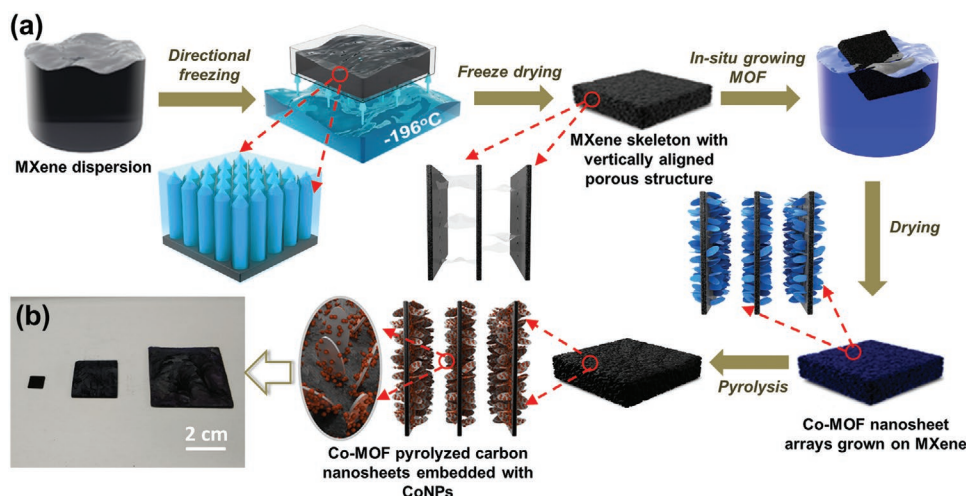
**ADVANCED
FUNCTIONAL
MATERIALS**
www.afm-journal.de

efficient solar to vapor generation is to develop a solar absorber possessing the following characteristics: 1) the solar absorber is capable of efficiently absorbing light across the entire solar spectrum (300–2500 nm);[21–23] 2) the solar absorber has a high light to heat conversion efficiency, which promotes the conversion of absorbed solar energy into thermal energy;[24,25] 3) the solar absorber has low thermal conductivity to suppress heat loss, arising from conduction, convection, and radiation;[14,16] 4) the solar absorber has good wettability and possesses a porous structure to enable continuous and efficient water transport and evaporation; 5) the solar absorber is mechanically robust and chemically stable to enable its use for practical applications in harsh hypersaline seawater and continuous irradiation conditions over prolonged periods of time: 6) the solar absorber or solar desalination system is provided with salt-rejection properties to reject excess salts left from long-term evaporation.[26,27]

Over the past decade, two predominant categories of photothermal materials for solar absorbers have been heavily investigated, with these two categories of photothermal materials based on different photothermal mechanisms. Carbonaceous materials convert solar energy into heat through lattice vibrations,[28] while plasmonic nanoparticles use a plasmonic localized heating mechanism.[29–32] The former includes conventional carbon materials, such as biomass-derived amorphous carbon, carbon black and graphite,[16,33–36] and novel nanocarbon materials, including graphene and carbon nanotubes,[37–40] and are desirable for broadband light absorption due in part to the optical transitions of their π-band.[41] However, carbonaceous photothermal materials have inherent limitations when considered for use for solar-vapor generation. Carbon materials with an amorphous structure have low thermal conductivity, but suffer from low light to heat conversion efficiency, whereas nanocarbon materials with a polycyclic aromatic structure show the reverse trend.[42–44] The latter category of materials, plasmonic nanoparticles, have distributed sizes and multiple scattering centers, enabling an overall absorptivity higher than 95%.[1] The absorptivity has even been demonstrated to reach 99% in certain cases[45] due to the intense hybridized surface plasmon resonance.[46,47] However, plasmonic nanoparticles are known to be toxic and to be prone to instability, and are fiscally restrictive and require complex fabrication processes.[37,48,49] To date, both carbonaceous materials and plasmonic nanoparticles fail to fully meet all the basic requirements required for an ideal solar absorber to be used for practical solar desalination and sewage treatment applications.

In recent years, MXene, a new family of 2D materials, has demonstrated promise for use as a solar absorber, outside of the two aforementioned categories of materials.[50–52] This material is derived from MAX phases, or layered hexagonal carbides and nitrides, where A is an A-group element, typically aluminum or gallium. MXene is fabricated by etching away this A-group element from the MAX phase, and can be defined by a general formula $M_{n+1}X_nT_x$, wherein M represents an early transition metal, X is either carbon or nitrogen, T represents surface termination groups (−O, −OH, and/or −F), and x denotes the number of functional termination groups. Due in part to its unique structure, MXene has demonstrated an internal light to heat conversion efficiency approaching 100%, and high light absorption across a broad range of wavelengths.[53] Furthermore, the plethora of hydrophilic terminal groups on the surface of MXene nanosheets enhance their wettability, which enables rapid water transport on their hydrophilic surfaces.[54–56] Pioneering works have already reported on the promising potential of MXene-based photothermal materials when used as solar absorbers in solar desalination applications.[57] However, MXene is still plagued by inherently undesirable characteristics, including high thermal conductivity,[52,58] moderate broadband light reflection,[59] and its tendency to be easily oxidized. These unfortunate tendencies limit the solar to thermal conversion efficiency of MXene-based materials for solar-vapor generation. Considerable effort has been put forth in addressing these concerns, including introducing a hierarchical crumpled structure,[59] microporous structure,[60] and Janus structure.[61] However, even with the introduction of these various structures, the solar-thermal conversion efficiency for the MXene-based solar absorber is still limited. Because the development of MXene-based materials for solar desalination is still in its infancy, there remains much room for improvement.

In this work, a cobalt nanoparticle (CoNP)-carbonaceous nanosheets/MXene foam (herein referred to as Co-CNS/M foam) is designed and fabricated with an ordered hierarchical structure using MXene nanosheets and cobalt-based metal–organic frameworks (Co-MOFs) as precursors. This foam comprises a 3D MXene microporous skeleton with vertically aligned MXene nanosheets, decorated with vertical arrays of 2D carbon nanoplates embedded with CoNPs. The rationale behind the integration of three categories of photothermal materials to generate this specific and unique multilevel hierarchical architecture is to enable the Co-CNS/M foam to possess five critical features. First, the vertical arrays of 2D carbon nanoplates derived from MOFs can suppress the incident light reflection through multiple light scattering and reflection, resulting in enhanced solar light absorption across a broad spectrum of wavelengths. Second, the photothermal mechanism combines the thermal vibration of molecules and plasmonic localized heating, which ensures a high light to heat conversion efficiency. Third, the amorphous carbon nanoplate arrays acting in conjunction with the porous skeleton architecture significantly reduces the thermal conductivity of the hybrid foam. Fourth, the vertically aligned porous structure with an intrinsically hydrophilic cell wall enables rapid water transport throughout the solar absorber. Fifth, the carbon nanoplate arrays on the surface of the MXene nanosheets significantly improve the chemical stability of the MXene-based skeleton in harsh conditions. Lastly, a polystyrene foam with a channel drilled through the foam, serving as a thermal insulating layer between the solar absorber and bulk water, can further suppress the heat loss and improve the salt-rejection ability of the entire solar desalination system. Based on all these critical features, the Co-CNS/M foam exhibits an external solar-thermal energy conversion efficiency up to 93.39% (average of 93.06%) under one sun irradiation intensity when acting as a solar absorber for water desalination, a figure of merit exceeding all other reported MXene-based photothermal materials to date, to the best of our knowledge. Furthermore, the water production rate suggests no obvious degradation under one sun irradiation for 10 days, 10 h illumination each day (a total of 100 h of irradiation), indicating

**ADVANCED
SCIENCE NEWS**
www.advancedsciencenews.com

**ADVANCED
FUNCTIONAL
MATERIALS**
www.afm-journal.de

Figure 1. a) Schematic illustration of the fabrication process of the Co-CNS/M foam. b) Optical image of different sizes of the as-prepared Co-CNS/M foams. (From left to right: 1 × 1 cm, 2.5 × 2.5 cm, and 5 × 5 cm. All samples have a thickness is 0.12 cm).

the reusability, long-term stability, and good salt-rejection capability of our MXene-based evaporation system.

2. Results and Discussion

The Co-CNS/M solar absorber was fabricated by growing Co-MOF (ZIF-L) directly onto the surface of a $Ti_3C_2T_x$ MXene skeleton possessing a vertically aligned porous architecture, followed by pyrolyzing the Co-MOF nanoplate into amorphous carbon nanoplate arrays embedded with CoNPs, as illustrated in **Figure 1**a. To obtain the delaminated and hydrophilic MXene nanosheets (≈2–4 µm in lateral dimension, and 1.8 nm in thickness; Figure S1, Supporting Information), Ti_3AlC_2 MAX was selectively etched and then exfoliated in distilled water and ethanol solution to obtain a stable MXene dispersion.[55,62,63] The addition of ethanol facilitates the formation of pure MXene foam with a vertically aligned porous structure during the subsequent directional freeze-drying process.[64] The MXene foam was then immersed into an aqueous precursor solution containing 2-methylimidazole and $Co(NO_3)_2 \cdot 6H_2O$, and gently stirred to grow Co-MOF nanoplate arrays onto the surface of MXene to obtain the Co-MOF decorated MXene foam (denoted as Co-MOF/M foam).[65] Subsequently, the Co-MOF/M foam was annealed at 450 °C for 2 h under inert argon gas to reduce the Co^{2+} liberated from the Co-MOF to ultrafine Co nanoparticles, and to convert the coordinated organic ligands into amorphous carbon nanoplates.[66,67] Figure 1b depicts a digital photograph of different sizes of the resultant all-black, Co-CNS/M hybrid foams (1 × 1 cm, 2.5 × 2.5 cm, 5 × 5 cm).

Materials characterization was conducted to elucidate more regarding the inherent nature of the foam as a result of its individual constituents. The microstructure of the as-prepared samples, including Co-CNS/M, Co-MOF/M, and pure MXene foams were first characterized using scanning electron microscopy (SEM). As illustrated in **Figure 2**a and Figures S2 and S3, Supporting Information, all foams exhibit vertically aligned microchannels, with the microchannel width approximately 30–50 µm. Furthermore, the magnified SEM images shown

in Figure 2b and Figure S3b, Supporting Information, indicate that the channel wall in all MXene-based foams exhibit a lamellar structure. It is noted that after the growth of Co-MOFs, the hierarchical structure of the leaf-like nanoplates are densely and uniformly covered on both surfaces of the channel walls in the Co-MOF/M foam, as seen in the magnified SEM image (Figure S2b, Supporting Information). In addition, these leaf-like nanoplate structures were also observed to remain intact in the Co-CNS/M foams (Figure 2c), which were subjected to a 450 °C for 2 h under argon to trigger the controlled pyrolysis of Co-MOF. The structural and crystal integrity of the as-synthesized Co-MOF nanoplates in the Co-MOF/M foam were confirmed through powder X-ray diffraction (XRD) characterization (Figure 2i).[65]

Transmission electron microscopy (TEM) was used to gather further insight into the detailed structural and morphological features of the carbon nanoplates in the Co-CNS/M foam. As seen in Figure 2d, a plethora of black nanoparticles are uniformly distributed in one leaf-like carbon nanoplate derived from Co-MOFs. The high-resolution TEM images in Figure 2e reveal that the carbonic structure around the nanoparticles is disordered, indicative of its amorphous carbon structure.[67] The interspacing of lattice fringe in the nanoparticle was found to be 0.21 nm, which can be attributed to the (111) plane of the face-centered cubic metal, Co.[68] Corresponding energy-dispersive X-ray spectroscopy (EDS) elemental mapping results (Figure 2f and Figure S4, Supporting Information) illustrate the homogenous distribution of Co elements over the carbon nanoplates and the entirety of the Co-CNS/M hybrid foam. X-ray photoelectron spectroscopy (XPS) was also conducted to analyze the surface chemical composition of the Co-CNS/M hybrid foam. The survey spectrum reveals the Co 2p, C 1s, N 1s, Ti 2p, Ti 3p, and O 1s peaks found in the Co-CNS/M foam (Figure 2g). A high-resolution Co 2p spectrum is provided in Figure 2h, and can be deconvoluted into two characteristic peaks, located at 778.6 and 780.4 eV, confirming the existence of metallic Co, and the presence of the Co—N bond.[69] A secondary characteristic peak attributed to metallic Co was also found at 44.3° in the Co-CNS/M foam, which was not revealed in the Co-MOF/M foam
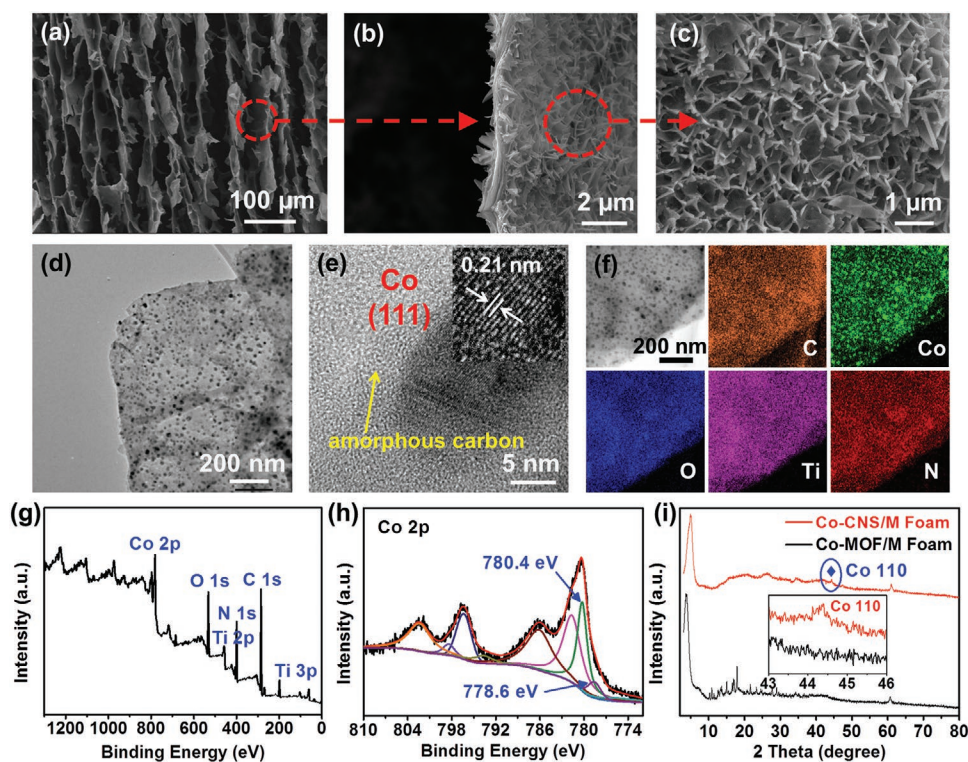
Figure 2. a) A cross-sectional SEM image of the Co-CNS/M foam depicting the vertically aligned porous structure. b,c) Magnified SEM images of the Co-CNS/M foam showing the carbon nanoplate arrays grown on the cell wall of the porous structure. d) TEM image, e) magnified TEM image, and f) EDS elemental mapping images of one carbon nanoplate structure within the Co-CNS/M foam, indicating the presence of amorphous carbon and CoNP in the carbon nanoplate structure. g) XPS survey spectra of the Co-CNS/M foam. h) High-resolution XPS spectrum of Co 2p of the Co-CNS/M foam. i) XRD patterns of the Co-MOF/M and Co-CNS/M foams.

(Figure 2i). These aforementioned characterizations confirm the presence of CoNP (with dimensions ≈20 nm) distributed within the amorphous carbon nanoplates, which are uniformly grown over the entirety of the MXene skeleton within the Co-CNS/M foam.

Following material level characterization, the specific features required for efficient solar absorbers were further investigated and compared between the pure MXene and Co-CNS/M foams. Thermal conductivity is one such factor that impacts the efficiency of solar-vapor generation, as low thermal conductivity enables the localization of the converted heat into a small region near the solar absorber without heating the water.[70] The equivalent thermal conductivity of a dry Co-CNS/M foam was calculated to be ≈0.242 W m^{-1} K^{-1}, lower than that of the MXene (≈0.345 W m^{-1} K^{-1}). Detailed calculations regarding thermal conductivity can be found under Methods. When the samples were fully saturated with water, the equivalent thermal conductivity of the wet Co-CNS/M foam (≈0.591 W m^{-1} K^{-1}) was still lower than that of pure the MXene foam (≈0.790 W m^{-1} K^{-1}). While MXene nanosheets intrinsically possess high thermal conductivity,[58,52] the low thermal conductivity observed in the Co-CNS/M foam can be attributed to the amorphous carbon nanoplate arrays grown on the MXene surface, in addition to its hierarchical porous architecture.[21,71,72]

Optical absorption is another critical feature impacting solar-vapor generation. It is expected that the carbon nanoplate arrays on the MXene surface can induce strong light scattering and multiple internal reflections of incident light, trapping the incident light within the Co-CNS/M foam which subsequently improves light absorption.[37,73,74] To quantify the optical absorption properties of the MXene-based solar absorbers, optical absorption, reflection, and transmittance spectrum characterizations were conducted using an ultraviolet-visible, near-infrared (UV–vis–NIR) spectrophotometer equipped with an integrating sphere, as illustrated in **Figure 3**a ,b and Figure S5, Supporting Information. While both the MXene and Co-CNS/M foam exhibited relatively low transmittances throughout the entirety of the solar spectrum (Figure S5, Supporting Information), the incident light irradiated on the Co-CNS/M foam exhibited a significantly lower reflection (Figure 3b). Correspondingly, the Co-CNS/M hybrid foam had an average absorption over 98% in the visible to near-infrared range, and over 97% from 200 nm to 2000 nm wavelength in the solar spectrum, higher than those of the pure MXene foam (Figure 3a). Based on the normalized spectral solar irradiance density, the absorbed solar energy of Co-CNS/M hybrid foam was calculated to be 97.5%, higher than that of the MXene foam (≈95%). The decrease of light absorption in the wavelength above 2000 nm is mainly attributed to the physical properties of the MXene nanosheet, as discussed in detail in Note S3, Supporting Information.

Following optical absorption characterization, the solar-thermal properties of the MXene-based solar absorbers were systematically examined. The surface temperature variations of pure MXene and Co-CNS/M foams in their dry states under one
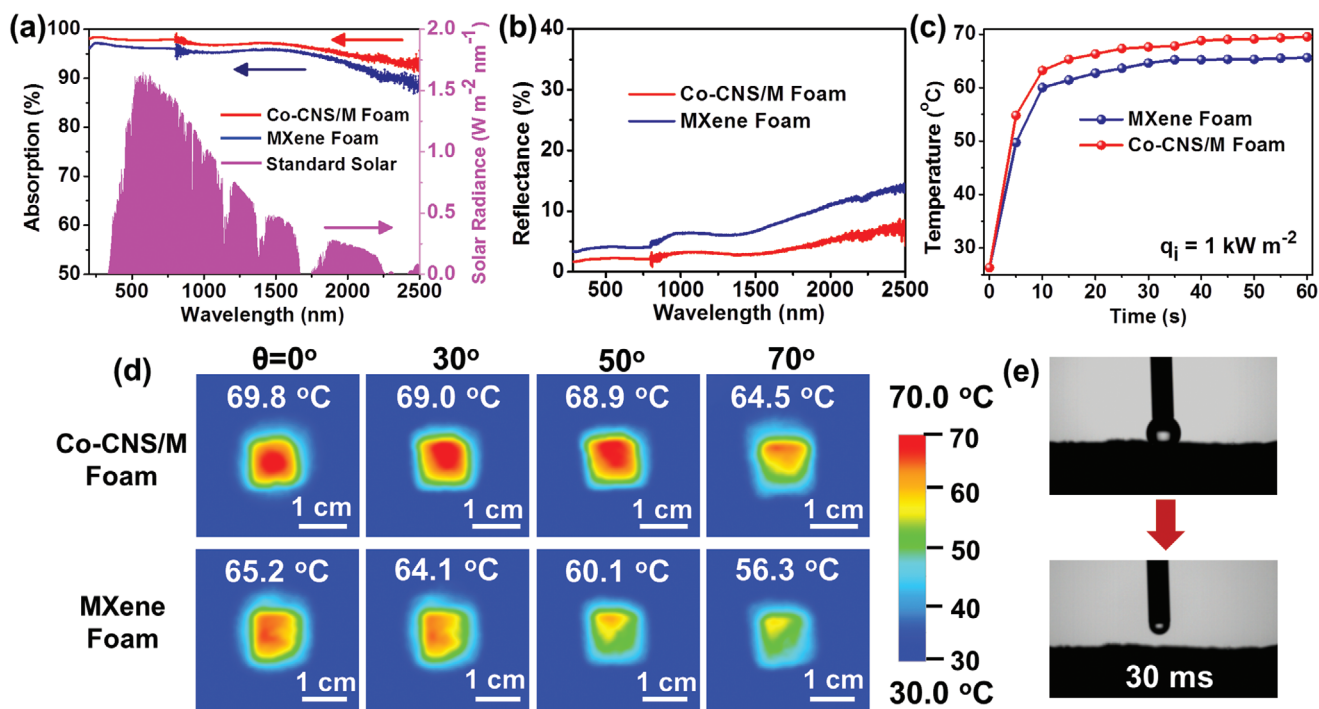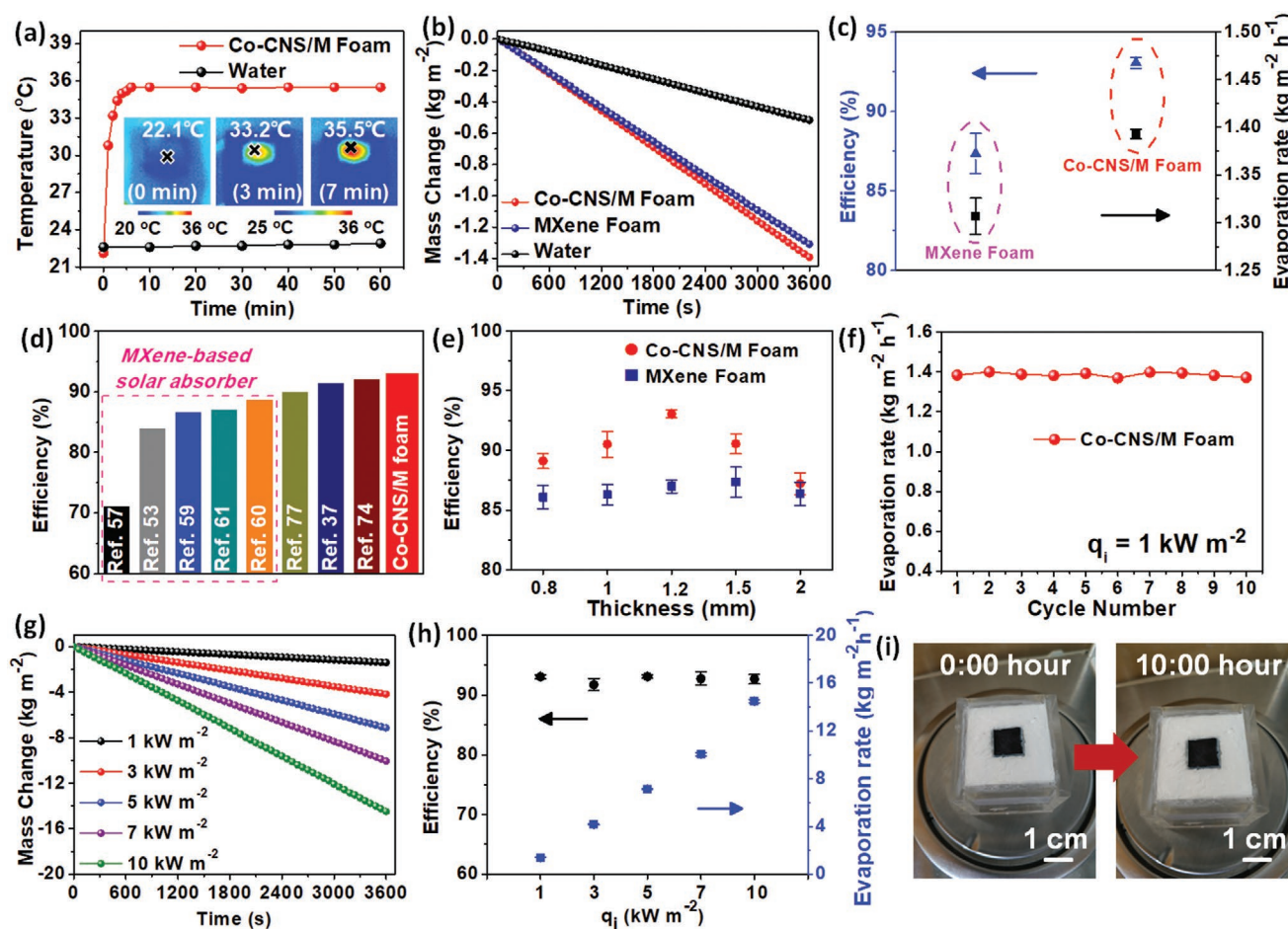
Figure 3. a) Absorption and b) reflectance spectra of the MXene foam (blue) and Co-CNS/M foam (red) with thicknesses of 0.12 cm. The normalized spectral solar irradiance density of the air mass 1.5 global (AM 1.5) tilt solar spectrum is shown in the pink curve depicted in (a). c) Measured surface temperature variation profiles of the MXene and Co-CNS/M foam under one sun solar irradiation. d) Infrared thermal images of MXene and Co-CNS/M foam at incident angles of 70°, 50°, 30°, and 0° under one sun solar irradiation. e) Time-dependent changes of contact angle of the Co-CNS/M foam.

sun illumination (1 kW m^{-2}) were recorded using IR thermal imaging, as shown in Figure 3c and Figure S6, Supporting Information. The light to heat performance can be quantified by the temperature delta between room temperature (T_r) and the surface equilibrium temperature of the samples (T_c).[59] It is observed that the surface temperatures of both pure MXene and Co-CNS/M foams exhibit a rapid increase upon light irradiation, indicating good photothermal performance of the MXene nanosheets. A stable T_c of 69.5 °C was achieved within 60 s for the Co-CNS/M foam, whereas the corresponding T_c reach of the MXene foam was only 65.6 °C (Figure 3c). Surface temperature deltas under light irradiation with various incident angles were also measured to investigate the directional dependence of the solar absorbers (Figure 3d). The surface temperature of the Co-CNS/M foam under one solar irradiation for 1 min shows a slight decrease from 69.8 to 68.9 °C when the incident angle increases from 0 to 50°. At a larger incident angle of 70°, corresponding to a significantly reduced projected area, the Co-CNS/M foam still exhibited a stable surface temperature of 64.5 °C, indicating low dependency of solar-thermal conversion on lighting direction. This surface temperature at a 70° is comparable to the surface temperature of the MXene foam with light directly incident to its surface. The enhanced light to heat performance of the Co-CNS/M foam can be attributed to its unique hierarchical structure. The carbon nanoplate arrays grown on the Co-CNS/M foam results in more light trapping and absorption, and thus improved equilibrium temperature in contrast with the pure MXene foam.[37] Furthermore, the plasmonic localized heating generated within the CoNPs embedded in the carbon nanoplates under solar irradiation also increases

the surface temperature of the Co-CNS/M foam (Figure S7, Supporting Information).

This unique hierarchical structure also endows the Co-CNS/M foam with its water transfer ability. The wettability of the Co-CNS/M foam was characterized by its water contact angle, which is strongly impacted by the composition and micro/nanostructure of the material surface. As illustrated in Figure 3e, a drop of water was immediately absorbed by the Co-CNS/M foam in less than 30 ms after coming in contact with the sample surface, indicative of the good hydrophilicity of the Co-CNS/M foam. This wetting ability, in conjunction with the continuous water pathway supplied from the primary microchannel structure in the vertically aligned MXene skeleton (Figure 2a) and the high specific surface area due to the secondary nanostructure of carbon nanoplates arrays (Figure S8, Supporting Information), enables rapid water supply and efficient evaporation when using the Co-CNS/M foam.[64,75–77]

Taking the physical and structural properties of Co-CNS/M foam into account, the solar steam generation and desalination performances were subsequently investigated. As illustrated in Figure S9, Supporting Information, the custom-made steam-generation device used in this work can be broken down into four parts: 1) a PMMA container used to store water; 2) a square solar absorber (1 × 1 cm) with all four sides sealed by nail-free glue to fit into the water container, while preventing water evaporation from sidewalls; 3) a polystyrene foam (1.6 cm thick) with a channel (0.5 cm width) drilled through the foam, serving as a thermal insulating layer between the solar absorber and bulk water to further suppress the heat loss. The minute gap between the polystyrene foam and the container was also tightly sealed

**ADVANCED
SCIENCE NEWS**

www.advancedsciencenews.com

**ADVANCED
FUNCTIONAL
MATERIALS**

www.afm-journal.de

Figure 4. a) Surface temperature change as a function of irradiation time for the Co-CNS/M foam when floating on a water bath under one sun solar illumination. The inset depicts the IR thermal images showing the temperature distribution within the Co-CNS/M foam. b) Mass change of water over time of the Co-CNS/M and pure MXene foams under one sun solar illumination. c) Evaporation rates and evaporation efficiencies of the Co-CNS/M and pure MXene foams calculated from (b). Error bars indicate the standard deviation of the measurements (three devices were measured for each sample). d) Comparison of evaporation efficiencies between the Co-CNS/M foam and previous reports when under one sun irradiation. e) Comparison of evaporation efficiencies between MXene and Co-CNS/M foams at various thicknesses. f) Reusability of the Co-CNS/M foam under 1 solar irradiation over 10 cycles; each cycle was continuously tested for 10 h. g) Mass change of water over time for the Co-CNS/M foam under different light irradiation intensities. h) Evaporation rates and evaporation efficiencies of the Co-CNS/M foam under different light irradiation intensities calculated from (g). i) Optical photographs of the surface of Co-CNS/M foam before and after floating on a 3.5 wt% NaCl simulated seawater bath under one sun solar illumination for 10 h.

to avoid evaporation through the gap; 4) the hydrophilic non-wovens connecting the channel in the polystyrene insulating layer with the water to continuously feed the solar absorber with water via capillary force as well as advect and diffuse concentrated salt down back into the water. A solar simulator was used as the light source (Figure S10, Supporting Information). As shown in the temperature profile in **Figure 4**a, a large temperature differential can be observed between the top surface of the Co-CNS/M foam and the underlying water under one solar illumination of 1 kW m^{-2} within 7 min. The surface temperature of the Co-CNS/M foam rose from the room temperature to 33.2 °C in 3 min, then remained relatively constant, whereas the temperature of the underlying water surface increased by only 0.3 °C over the entire irradiation process. This indicates that heat loss can be greatly suppressed using the proposed testing and thermal isolation design, which is critical for localizing the converted heat in the solar absorber of the Co-CNS/M foam.[2,64]

Typical solar-thermal evaporation curves of the pure MXene and Co-CNS/M foams with thicknesses of 1.2 mm were measured, showing the mass change as a function of time under solar illumination of 1 kW m^{-2}. Corresponding water evaporation rates were calculated from the slope of the curves (Figure 4b). It is noted that the dark evaporation amount of the samples (Figure S11, Supporting Information) in this work are attributed to background noise, but were not subtracted, as they provide valuable insight into the ambient operating conditions as well as serving as a baseline for the evaporation rate (detailed discussions in Note S1, Supporting Information). The solar absorber using the Co-CNS/M foam had an average water evaporation rate of 1.393 kg m^{-1} h^{-1}, which was higher than that of the pure MXene foam (1.306 kg m^{-2} h^{-1}). The baseline evaporation rate without the aid of a solar absorber was 0.51 kg m^{-2} h^{-1}. The corresponding solar-vapor conversion efficiency of the Co-CNS/M foam was calculated to be 93.39%

(average value of 93.06%) under one sun irradiation (Figure 4c), a value amongst the highest of all solar absorbers (Table S1, Supporting Information), and significantly higher than all previously published MXene-based solar absorbers (Figure 4d). The Co-CNS/M hybrid foams with thicknesses ranging from 0.8 to 2 mm all exhibited higher solar-vapor conversion efficiencies than those of the baseline MXene foam (Figure 4e), further validating the material and structural advantages derived from using Co-CNS/M in solar-vapor generation. The reduction of solar-vapor conversion efficiency in the pure MXene foam is largely attributed to heat loss to the environment and underlying water, which includes radiative heat loss to the environment, convective heat loss to the environment, and conductive heat loss to the underlying water.[19] These sources of heat loss in the Co-CNS/M foam are calculated to be 1.9%, 1.5%, and 0.87%, respectively (detailed calculation shown in Note S2, Supporting Information). As a result of the minimal heat loss, the theoretical solar-steam generation efficiency is calculated to be 93.23% (detailed calculation shown in Note S2, Supporting Information), which is consistent with the empirically derived value of 93.39%.

In addition, the stability and durability of solar absorbers is also critical, as real-world applications often occur under harsh environments over long durations of irradiation. To characterize the reusability of the pure MXene and Co-CNS/M foam, the solar water evaporation tests were conducted repeatedly using the same samples. During each cycle, water was continuously evaporated under one solar irradiation for 10 h, after which and the solar absorbers were taken out to dry. After replenishing the water, the dried solar absorbers were assembled into the container for the next cycle test. As illustrated in Figure S12, Supporting Information, the specific water production rate of the pure MXene foam shows a significant decrease only after irradiation for 2 h due to the oxidation and degradation of the MXene skeleton which occurs under aqueous condition.[78,79] In contrast, the Co-CNS/M foam shows no change in its structure and retains a high evaporation rate of approximately 1.38 kg m^{-2} h^{-1} even after 10 cycles, equating to 100 h of light irradiation (Figure 4f). This improved stability can be attributed to the MOF-derived carbon nanosheet arrays grafted onto the surface of the MXene nanosheets, which can prevent the MXene from directly coming into contact with the water. The evaporation rates and corresponding efficiencies of the Co-CNS/M foam under various light irradiation intensities spanning from 1 to 10 kW m^{-2} were also measured and are shown in Figure 4g,h. Overall, the solar absorber performed well, even under high light irradiation intensities. The evaporation rates of the Co-CNS/M foam were seen to increase corresponding to increases in light intensity, with the respective energy conversion efficiencies all measured to be greater than 91% under varied light (Figure 4h).

Moreover, the salt-rejection capability of the evaporation structure composed of a top Co-CNS/M foam and a bottom polystyrene foam was characterized by two complementary experiments. First, the evaporation structure was floated in a 3.5 wt% NaCl simulated seawater reservoir and was irradiated under one sun. Notably, no salt crystal or white solid was observed to form on the surface of Co-CNS/M foam after continuously illuminating for 10 h (Figure 4i), indicating the good salt-rejection ability of the evaporation system. In addition, the evaporation structure was placed in 3.5 wt% NaCl simulated seawater, and 0.15 grams of additional solid NaCl was placed directly on the top surface of Co-CNS/M foam. After one sun irradiation over ≈2.5 h, the evaporation structure can fully reject the salt and no solid salt was left on the surface of Co-CNS/M foam (Figure S13, Supporting Information), indicating that the evaporation structure can dissolve and reject salt deposits even under constant sunlight. This excellent salt-rejection ability is mainly attributed to the polystyrene foam beneath the Co-CNS/M foam. The hydrophilic nonwoven connecting the channel in the hydrophobic polystyrene layer can advect and diffuse concentrated salt down back into the water.[80]

The highly efficient solar-vapor generation of the solar absorber using the Co-CNS/M foam is due largely in part to its unique hierarchical porous structure and inherent properties of its individual constituents (**Figure 5**). The 2D MXene nanosheets and carbon nanosheets enable broadband sunlight absorption, while the vertically aligned porous skeleton and dense nanoplate arrays suppress incident light reflection through strong light scattering and multiple reflections within the hierarchical structure, further enhancing light absorption. The absorbed light is immediately and efficiently converted into heat through thermal vibrations in the MXene and amorphous carbon nanosheets, and through plasmonic localized heating of CoNPs embedded within the carbon nanoplate arrays. The low thermal conductivity of the amorphous carbon nanoplate arrays greatly suppress heat loss to the surrounding environment and underlying water, which localizes the converted heat to optimize thermal utilization. Lastly, the vertically aligned porous microchannel structure with an intrinsically hydrophilic cell wall provides smooth and continuous pathways for water transportation and vapor evaporation, while the large specific surface area induced by the carbon nanoplate arrays offers abundant water stockpile sites and vaporization nuclei.[37] These factors are directly responsible for the high solar-vapor generation efficiency observed using the Co-CNS/M foam.

To demonstrate the feasibility of the Co-CNS/M foam as a solar absorber for practical seawater desalination, a real seawater sample (collected from Bohai Sea, China) was employed as the saline solution, and the concentrations of four primary ions (Na^+, Mg^{2+}, Ca^{2+}, and K^+) in the saline solution before desalination and after desalination were monitored using a conductivity test (Figure S14, Supporting Information) and inductively coupled plasma spectroscopy, respectively. After desalination conducted by irradiating the Co-CNS/M foam with light intensities of 1 kW m^{-2}, the concentrations of all four targeted metal ions decreased by three to four orders of magnitude, and were all significantly lower than the safe salinity levels defined by standards set by the World Health Organization (WHO) and the US Environmental Protection Agency (EPA) (**Figure 6**a). Methyl orange and methylene blue were also added into the water sample to act as pollutants to further evaluate the sewage treatment ability of the Co-CNS/M foam. As shown in Figure 6b, the strong absorption peaks belonging to methyl orange (≈465 nm) and methylene blue (≈665 nm) were almost completely eliminated after the sewage treatment, with negligible residual contamination in the resultant clean water.
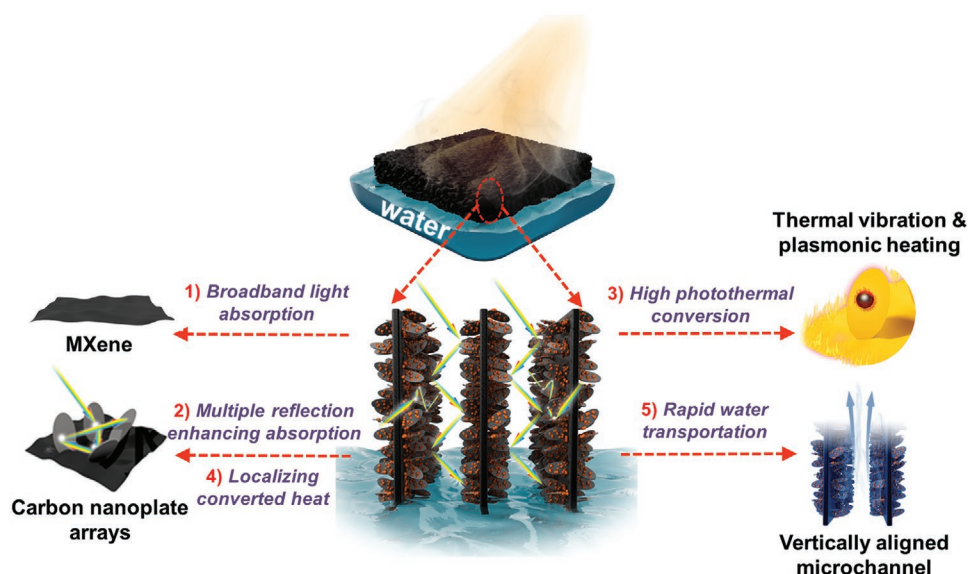
Figure 5. Schematic of the highly efficient solar-vapor generation from the solar absorber of Co-CNS/M foam.

To further demonstrate the real performance under true factors such as the varied sunlight intensity and incident angles, a solar desalination experiment was conducted under outdoor natural sunlight (Figure S15, Supporting Information) for half a day (8:00–20:00, 17 June 2020, Tianjin, China) using a large-scale Co-CNS/M foam (16 cm × 16 cm) assembled with polystyrene foam as a steam generator. The time-dependent mass change was monitored together with ambient sunlight intensity (Figure 6c). From 10:00 to 15:30, the solar flux remained at a high value of about 500–900 W m^{-2} and the mass changes of the water showed a continuous increase in this period, regardless of the position of the sun. The total evaporation during this half daytime test (12 h) is measured to be 5.32 kg m^{-2}.
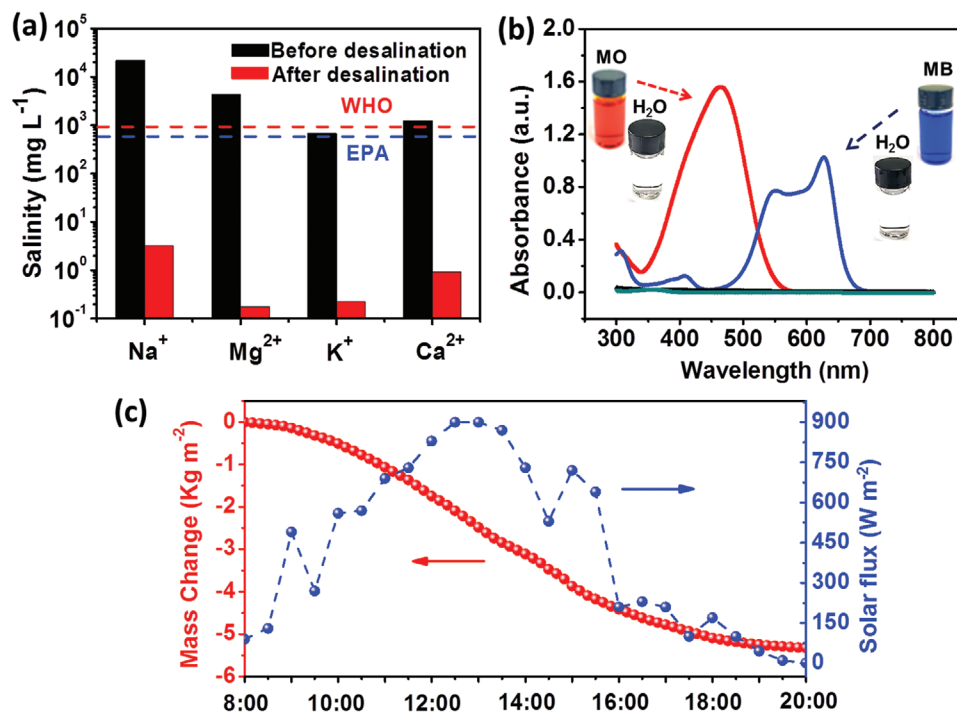
Figure 6. a) The measured concentrations of Na$^+$, K$^+$, Mg^{2+}, and Ca^{2+} in an actual seawater sample before and after desalination. The dashed red and blue lines refer to the WHO and EPA standards for drinkable water, respectively. b) Simulated sewage treatment performance of the Co-CNS/M foam under solar illumination. c) 12 h (17 June 2020, Tianjin, China) continuous measurement of the solar flux and clean water generation using a large-scale Co-CNS/M foam (16 cm × 16 cm) assembled as a steam generator. The ambient solar flux (blue line) and mass change of the water (red line) using a covered device were recorded from 8:00 am to 8:00 pm.

**ADVANCED
SCIENCE NEWS**

www.advancedsciencenews.com

**ADVANCED
FUNCTIONAL
MATERIALS**

www.afm-journal.de

3. Conclusion

A hierarchical Co-CNS/M foam was designed and fabricated by introducing arrays of CoNPs embedded amorphous carbon nanoplates onto a porous MXene skeleton with vertically aligned microchannel structure. The foam leverages the material properties of its individual constituents and a unique hierarchical structure, which when combined, addresses the basic feature requirements for ideal solar absorbers. As a result, ultrahigh broadband light absorption, efficient light to heat conversion, suppression of heat loss, rapid water transportation, and improve resistance to corrosion and oxidation are observed. Furthermore, the Co-CNS/M foam exhibits a high solar-vapor generation rate with an energy efficiency of up to ≈93.39% under one sun illumination, and was demonstrated to be highly stable and re-useable. The feasibility of the Co-CNS/M foam for practical seawater desalination and sewage treatment was also successfully demonstrated. This strategy opens an avenue for the development of a new category of MXene-based solar absorbers.

4. Experimental Section

Synthesis of $Ti_3C_2T_x$ MXene: $Ti_3C_2T_x$ was synthesized by etching the Ti_3AlC_2 MAX phase in LiF using HCl. In a typical synthesis, 2 g LiF was added to 20 mL of 9 mL HCl under sonication for 30 min. Subsequently, 2 g of Ti_3AlC_2 was slowly added into the solution over the course of 5 min at 35 °C, followed by magnetic stirring for 24 h. The resultant solution was centrifuged at 3500 rpm using deionized water several times until the supernatant pH reached ≈5. Then 40mL of ethanol was added to the precipitate, which was sonicated for 30 min and following centrifuged for 5 min at 3500 rpm. The final MXene powder was obtained after freeze-drying the collected supernatant.

Preparation of Vertically Aligned MXene Foam: MXene solution (60 mg mL^{-1}) was obtained by mixing MXene powder with distilled water under oscillation and sonification for 5 min. After mixing the powder, a certain amount of ethanol was added into the solution and then removed and placed into Teflon molds. These molds were placed on the surface of liquid nitrogen for 10 min for directional freeze casting through the bottom to the top.

Preparation of Co-CNS/M Hybrid Foam: Co-MOF was grown on the surface of the MXene foam according to a previously reported method with some modification.[65] 0.552 g of $Co(NO_3)_2 \cdot 6H_2O$ and 1.303 g of 2-Methylimidazole (2-MIM) were dissolved in 40 mL deionized water, respectively. The MXene foam was subsequently poured into and immersed in the mixture of the above two solutions under magnetic stirring at room temperature. After 90 min, the sample was taken out, washed with distilled water, and dried for further usage. Lastly, the foam sample was annealed under Ar at 450 °C for 2 h with a ramp rate of 2 °C min^{-1}.

Solar-Vapor Generation Experiments: The water evaporation performance experiments were conducted using a solar simulator (7ILX500P, SOFN Instruments Co., LTD, with an optical filter for the standard AM-1.5 spectrum) outputting a simulated solar flux of 1–10 kW m^{-2}. The size of the light spot was controlled via an aperture, ensuring the spot size was equal to the size of the sample. The solar flux was measured using a solar power meter (CEL-NP 2000 Full spectrum Strong light power meter). The temperature was measured using an infrared thermal imager (Testo 869, Testo SE & Co. KGaA) and thermocouple. The mass change of water was measured using a laboratory balance with 0.1 mg resolution (OHAUS, AX224ZH) while the steam generation was in a steady state. Experiments were typically conducted at an ambient temperature between 25 and 26 °C and humidity between 55% and 60%.

Calculation of Solar Absorption of Materials: The absorbance of samples was measured and calculated from their UV–vis–IR diffuse reflectance spectra.[81] The solar absorption energy of the samples can be calculated by the equation:

$$A = \frac{\int (1-R) \cdot S \cdot d\lambda}{\int S \cdot d\lambda} \tag{1}$$

wherein A is the solar absorption; R is reflectance of the sample, S is the solar spectral irradiance (W m^{-2} nm^{-1}), and λ is the wavelength (nm). Here, $(1 - R) \cdot S$ represents the sample absorption of solar spectral irradiance.

Thermal Conductivity Measurements: The thermal conductivities of the MXene foam and Co-CNS/M foam were measured according to previously published literature.[19] In detail, the samples were sandwiched between two glass slides, followed by the sandwiched samples being placed between a hot plate and a glass slide with ice on top. The temperature distribution along the thickness of the sample was monitored using a thermocouple and an IR camera. The Fourier equation was used to calculate the thermal conductivity of each sample:

$$q' = K \frac{\Delta T}{\Delta X} \tag{2}$$

Since the thermal conductivity (K) is known for the glass slides (1.05 W m^{-1} K^{-1} was used), the heat flux q' per unit area can be calculated. The thermal conductivity of the samples was calculated under the assumption that the samples and the glass slides experience the same heat flux.

Characterizations: SEM images were characterized using a field-emission scanning electron microscopy (JSM-7800). XPS spectra were obtained using an ESCALAB 250Xi system from Thermo Scientific. XRD patterns were acquired using a Rigaku D/max 2200 pc diffractometer under Cu Kα radiation. TEM images were captured using a transmission electron microscope (JEM-2800, Japan). The transmittance (T) and reflectance (R) spectra were measured using a Cary 5000 UV–vis–NIR spectrophotometer equipped with an integrating sphere, with the absorption calculated by the equation $A = 1 - R - T$. The nitrogen adsorption/desorption analysis at 77 K using a Micromeritics ASAP 2020 was conducted to calculate the specific surface area of the samples using the Brunauer–Emmett–Teller (BET) method. Wettability of the sample was characterized by water contact angles taken using a dynamic contact angle measuring instrument (JC2000D3M). The surface temperature and IR-images of the samples were measured and taken using an infrared thermal imager (Testo 869, Testo SE & Co. KGaA). The concentration of Na$^+$, K$^+$, Ca^{2+}, and Mg^{2+} were collected by atomic emission spectrometry with inductively coupled plasma (ICP-AES) using Thermo Fisher Icap 7400. The ultraviolet-visible absorbance spectra of simulated sewage and condensed water were tested using a Shimadzu UV-2600 spectrophotometer.

Supporting Information

Supporting Information is available from the Wiley Online Library or from the author.

Acknowledgements

Conflict of Interest

The authors declare no conflict of interest.

[1] L. Zhou, Y. L. Tan, J. Wang, W. Xu, Y. Yuan, W. Cai, S. Zhu, J. Zhu, *Nat. Photonics* **2016**, *10*, 393.

[2] W. Xu, X. Hu, S. Zhuang, Y. Wang, X. Li, L. Zhou, S. Zhu, J. Zhu, *Adv. Energy Mater.* **2018**, *8*, 1702884.

[3] M. W. Higgins, A. R. S. Rahmaan, R. R. Devarapalli, M. V. Shelke, N. Jha, *Sol. Energy* **2018**, *159*, 800.

[4] X. Huang, Y.-H. Yu, O. L. De Llergo, S. M. Marquez, Z. Cheng, *RSC Adv.* **2017**, *7*, 9495.

[5] N. Xu, J. Li, Y. Wang, C. Fang, X. Li, Y. Wang, L. Zhou, B. Zhu, Z. Wu, S. Zhu, J. Zhu, *Sci. Adv.* **2019**, *5*, eaaw7013.

[6] Y. Zeng, J. Yao, B. A. Horri, K. Wang, Y. Wu, D. Li, H. Wang, *Energy Environ. Sci.* **2011**, *4*, 4074.

[7] X. Wang, X. Li, G. Liu, J. Li, X. Hu, N. Xu, W. Zhao, B. Zhu, J. Zhu, *Angew. Chem., Int. Ed.* **2019**, *58*, 12054.

[8] S. D. Stranks, H. J. Snaith, *Nat. Nanotechnol.* **2015**, *10*, 391.

[9] L. Zhou, S. Zhuang, C. He, Y. Tan, Z. Wang, J. Zhu, *Nano Energy* **2017**, *32*, 195.

[10] X. Fan, Y. Ding, Y. Liu, J. Liang, Y. Chen, *ACS Nano* **2019**, *13*, 8124.

[11] Z. Wang, Z. Tong, Q. Ye, H. Hu, X. Nie, C. Yan, W. Shang, C. Song, J. Wu, J. Wang, H. Bao, P. Tao, T. Deng, *Nat. Commun.* **2017**, *8*, 1478.

[12] Y. Fu, G. Wang, T. Mei, J. Li, J. Wang, X. Wang, *ACS Sustainable Chem. Eng.* **2017**, *5*, 4665.

[13] M. Gao, C. K. Peh, H. T. Phan, L. Zhu, G. W. Ho, *Adv. Energy Mater.* **2018**, *8*, 1800711.

[14] Q. Jiang, L. Tian, K. K. Liu, S. Tadepalli, R. Raliya, P. Biswas, R. R. Naik, S. Singamaneni, *Adv. Mater.* **2016**, *28*, 9400.

[15] L. Zhu, M. Gao, C. K. N. Peh, X. Wang, G. W. Ho, *Adv. Energy Mater.* **2018**, *8*, 1702149.

[16] H. Ghasemi, G. Ni, A. M. Marconnet, J. Loomis, S. Yerci, N. Miljkovic, G. Chen, *Nat. Commun.* **2014**, *5*, 4449.

[17] X. Zhou, F. Zhao, Y. Guo, B. Rosenberger, G. Yu, *Sci. Adv.* **2019**, *5*, eaaw5484.

[18] F. Zhao, X. Zhou, Y. Shi, X. Qian, M. Alexander, X. Zhao, S. Mendez, R. Yang, L. Qu, G. Yu, *Nat. Nanotechnol.* **2018**, *13*, 489.

[19] Y. Yang, R. Zhao, T. Zhang, K. Zhao, P. Xiao, Y. Ma, P. M. Ajayan, G. Shi, Y. Chen, *ACS Nano* **2018**, *12*, 829.

[20] H. Song, Y. Liu, Z. Liu, M. H. Singer, C. Li, A. R. Cheney, D. Ji, L. Zhou, N. Zhang, X. Zeng, Z. Bei, Z. Yu, S. Jiang, Q. Gan, *Adv. Sci.* **2018**, *5*, 1800222.

[21] P. Wang, *Environ. Sci.: Nano* **2018**, *5*, 1078.

[22] C. Xing, D. Huang, S. Chen, Q. Huang, C. Zhou, Z. Peng, J. Li, X. Zhu, Y. Liu, Z. Liu, H. Chen, J. Zhao, L. Liu, F. Cheng, D. Fan, H. Zhang, *Adv. Sci.* **2019**, *6*, 1900531.

[23] J. Wang, Y. Li, L. Deng, N. Wei, Y. Weng, S. Dong, D. Qi, J. Qiu, X. Chen, T. Wu, *Adv. Mater.* **2017**, *29*, 1603730.

[24] X. Ma, W. Fang, Y. Guo, Z. Li, D. Chen, W. Ying, Z. Xu, C. Gao, X. Peng, *Small* **2019**, *15*, 1900354.

[25] C. Zhang, H. Q. Liang, Z. K. Xu, Z. Wang, *Adv. Sci.* **2019**, *6*, 1900883.

[26] C. Chen, Y. Kuang, L. Hu, *Joule* **2019**, *3*, 683.

[27] Y. Xia, Q. Hou, H. Jubaer, Y. Li, Y. Kang, S. Yuan, H. Liu, M. W. Woo, L. Zhang, L. Gao, H. Wang, X. Zhang, *Energy Environ. Sci.* **2019**, *12*, 1840.

[28] M. Gao, L. Zhu, C. K. Peh, G. W. Ho, *Energy Environ. Sci.* **2019**, *12*, 841.

[29] M. S. Zielinski, J. W. Choi, T. La Grange, M. Modestino, S. M. Hashemi, Y. Pu, S. Birkhold, J. A. Hubbell, D. Psaltis, *Nano Lett.* **2016**, *16*, 2159.

[30] E. Ye, K. Y. Win, H. R. Tan, M. Lin, C. P. Teng, A. Mlayah, M. Y. Han, *J. Am. Chem. Soc.* **2011**, *133*, 8506.

[31] M. Chen, Y. He, J. Huang, J. Zhu, *Energy Convers. Manage.* **2016**, *127*, 293.

[32] J. Liang, H. Liu, J. Yu, L. Zhou, J. Zhu, *Nanophotonics* **2019**, *8*, 771.

[33] G. Liu, J. Xu, K. Wang, *Nano Energy* **2017**, *41*, 269.

[34] Y. Liu, J. Chen, D. Guo, M. Cao, L. Jiang, *ACS Appl. Mater. Interfaces* **2015**, *7*, 13645.

[35] S. Loeb, C. Li, J. H. Kim, *Environ. Sci. Technol.* **2018**, *52*, 205.

[36] F. Wang, J. Liu, X. Fang, Z. Zhang, *Sol. Energy Mater. Sol. Cells* **2016**, *147*, 101.

[37] H. Ren, M. Tang, B. Guan, K. Wang, J. Yang, F. Wang, M. Wang, J. Shan, Z. Chen, D. Wei, H. Peng, Z. Liu, *Adv. Mater.* **2017**, *29*, 1702590.

[38] X. Yang, Y. Yang, L. Fu, M. Zou, Z. Li, A. Cao, Q. Yuan, *Adv. Funct. Mater.* **2018**, *28*, 1704505.

[39] Y. Wang, L. Zhang, P. Wang, *ACS Sustainable Chem. Eng.* **2016**, *4*, 1223.

[40] X. Zhou, F. Zhao, Y. Guo, Y. Zhang, G. Yu, *Energy Environ. Sci.* **2018**, *11*, 1985.

[41] Z. Wang, T. Horseman, A. P. Straub, N. Y. Yip, D. Li, M. Elimelech, S. Lin, *Sci. Adv.* **2019**, *5*, eaax0763.

[42] A. A. Balandin, *Nat. Mater.* **2011**, *10*, 569.

[43] G. Fugallo, A. Cepellotti, L. Paulatto, M. Lazzeri, N. Marzari, F. Mauri, *Nano Lett.* **2014**, *14*, 6109.

[44] Y. Zhu, S. Murali, W. Cai, X. Li, J. W. Suk, J. R. Potts, R. S. Ruoff, *Adv. Mater.* **2010**, *22*, 3906.

[45] L. Zhou, Y. Tan, D. Ji, B. Zhu, P. Zhang, J. Xu, Q. Gan, Z. Yu, J. Zhu, *Sci. Adv.* **2016**, *2*, e1501227.

[46] X. Ding, C. H. Liow, M. Zhang, R. Huang, C. Li, H. Shen, M. Liu, Y. Zou, N. Gao, Z. Zhang, Y. Li, Q. Wang, S. Li, J. Jiang, *J. Am. Chem. Soc.* **2014**, *136*, 15684.

[47] C. Y. Li, M. Meng, S. C. Huang, L. Li, S. R. Huang, S. Chen, L. Y. Meng, R. Panneerselvam, S. J. Zhang, B. Ren, Z. L. Yang, J. F. Li, Z. Q. Tian, *J. Am. Chem. Soc.* **2015**, *137*, 13784.

[48] W. Zhao, X. Liu, Y. Xu, S. Wang, T. Sun, S. Liu, X. Wu, Z. Xu, *RSC Adv.* **2016**, *6*, 35527.

[49] X. Wu, G. Y. Chen, G. Y. Zhang, X. Liu, H. Xu, *Adv. Sustainable Syst.* **2017**, *1*, 1700046.

[50] Z. Xie, Y. Duo, Z. Lin, T. Fan, C. Xing, L. Yu, R. Wang, M. Qiu, Y. Zhang, Y. Zhao, X. Yan, H. Zhang, *Adv. Sci.* **2020**, *7*, 1902236.

[51] H. Lin, Y. Wang, S. Gao, Y. Chen, J. Shi, *Adv. Mater.* **2018**, *30*, 1703284.

[52] Z. Li, H. Zhang, J. Han, Y. Chen, H. Lin, T. Yang, *Adv. Mater.* **2018**, *30*, 1706981.

[53] R. Li, L. Zhang, L. Shi, P. Wang, *ACS Nano* **2017**, *11*, 3752.

[54] T. H. Park, S. Yu, M. Koo, H. Kim, E. H. Kim, J. E. Park, B. Ok, B. Kim, S. H. Noh, C. Park, E. Kim, C. M. Koo, *ACS Nano* **2019**, *13*, 6835.

[55] M. Naguib, M. Kurtoglu, V. Presser, J. Lu, J. Niu, M. Heon, L. Hultman, Y. Gogotsi, M. W. Barsoum, *Adv. Mater.* **2011**, *23*, 4248.

[56] M. Naguib, V. N. Mochalin, M. W. Barsoum, Y. Gogotsi, *Adv. Mater.* **2014**, *26*, 992.

[57] J. Zhao, Y. Yang, C. Yang, Y. Tian, Y. Han, J. Liu, X. Yin, W. Que, *J. Mater. Chem. A* **2018**, *6*, 16196.

[58] J. Chen, X. Shi, N. Yu, X. Zhang, X. Du, J. Lin, *Materials* **2018**, *11*, 1701.

[59] K. Li, T. H. Chang, Z. Li, H. Yang, F. Fu, T. Li, J. S. Ho, P. Y. Chen, *Adv. Energy Mater.* **2019**, *9*, 1901687.

[60] X. Zhao, X.-J. Zha, J.-H. Pu, L. Bai, R.-Y. Bao, Z.-Y. Liu, M.-B. Yang, W. Yang, *J. Mater. Chem. A* **2019**, *7*, 10446.

[61] Q. Zhang, G. Yi, Z. Fu, H. Yu, S. Chen, X. Quan, *ACS Nano* **2019**, *13*, 13196.

[62] H. Li, X. Li, J. Liang, Y. Chen, *Adv. Energy Mater.* **2019**, *9*, 1803987.

[63] B. Anasori, M. R. Lukatskaya, Y. Gogotsi, *Nat. Rev. Mater.* **2017**, *2*, 16098.

[64] P. Zhang, J. Li, L. Lv, Y. Zhao, L. Qu, *ACS Nano* **2017**, *11*, 5087.

[65] X. Xu, F. Ran, Z. Fan, H. Lai, Z. Cheng, T. Lv, L. Shao, Y. Liu, *ACS Appl. Mater. Interfaces* **2019**, *11*, 13564.

[66] Z. Chen, Y. Ha, H. Jia, X. Yan, M. Chen, M. Liu, R. Wu, *Adv. Energy Mater.* **2019**, *9*, 1803918.

[67] R. Wang, J. Yang, X. Chen, Y. Zhao, W. Zhao, G. Qian, S. Li, Y. Xiao, H. Chen, Y. Ye, G. Zhou, F. Pan, *Adv. Energy Mater.* **2020**, *10*, 1903550.

[68] D. Fang, Y. Wang, C. Qian, X. Liu, X. Wang, S. Chen, S. Zhang, *Adv. Funct. Mater.* **2019**, *29*, 1900875.

[69] J. Li, C. Chen, Y. Chen, Z. Li, W. Xie, X. Zhang, M. Shao, M. Wei, *Adv. Energy Mater.* **2019**, *9*, 1901935.

[70] X. Hu, W. Xu, L. Zhou, Y. Tan, Y. Wang, S. Zhu, J. Zhu, *Adv. Mater.* **2017**, *29*, 1604031.

[71] A. J. Bullen, K. E. O'Hara, D. G. Cahill, *J. Appl. Phys.* **2000**, *88*, 6317.

[72] M. Shamsa, W. L. Liu, A. A. Balandin, C. Casiraghi, W. I. Milne, A. C. Ferrari, *Appl. Phys. Lett.* **2006**, *89*, 161921.

[73] X. Gao, H. Ren, J. Zhou, R. Du, C. Yin, R. Liu, H. Peng, L. Tong, Z. Liu, J. Zhang, *Chem. Mater.* **2017**, *29*, 5777.

[74] X. Wang, Q. Liu, S. Wu, B. Xu, H. Xu, *Adv. Mater.* **2019**, *31*, 1807716.

[75] N. Xu, X. Hu, W. Xu, X. Li, L. Zhou, S. Zhu, J. Zhu, *Adv. Mater.* **2017**, *29*, 1606762.

[76] P. Mu, Z. Zhang, W. Bai, J. He, H. Sun, Z. Zhu, W. Liang, A. Li, *Adv. Energy Mater.* **2019**, *9*, 1802158.

[77] B. Huo, D. Jiang, X. Cao, H. Liang, Z. Liu, C. Li, J. Liu, *Carbon* **2019**, *142*, 13.

[78] C. Xing, S. Chen, X. Liang, Q. Liu, M. Qu, Q. Zou, J. Li, H. Tan, L. Liu, D. Fan, H. Zhang, *ACS Appl. Mater. Interfaces* **2018**, *10*, 27631.

[79] Y. Chae, S. J. Kim, S. Y. Cho, J. Choi, K. Maleski, B. J. Lee, H. T. Jung, Y. Gogotsi, Y. Lee, C. W. Ahn, *Nanoscale* **2019**, *11*, 8387.

[80] G. Ni, S. H. Zandavi, S. M. Javid, S. V. Boriskina, T. A. Cooper, G. Chen, *Energy Environ. Sci.* **2018**, *11*, 1510.

[81] T. Lin, C. Yang, Z. Wang, H. Yin, X. Lü, F. Huang, J. Lin, X. Xie, M. Jiang, *Energy Environ. Sci.* **2014**, *7*, 967.